Purdue University
Purdue e-Pubs

CTRC Research Publications   Cooling Technologies Research Center

2019

Three-Dimensional Liquid-Vapor Interface Reconstruction from High-Speed Stereo Images during Pool Boiling

C. Mira-Hernandez
Purdue University

J. A. Weibel
Purdue University, jaweibel@purdue.edu

P. P. Vlachos
Purdue University

S V. Garimella
Purdue University, sureshg@purdue.edu

Follow this and additional works at: https://docs.lib.purdue.edu/coolingpubs

Three-dimensional liquid-vapor interface reconstruction from high-speed stereo images during pool boiling

Carolina Mira-Hernández, Justin A. Weibel, Pavlos P. Vlachos, Suresh V. Garimella

School of Mechanical Engineering, Purdue University

585 Purdue Mall, West Lafayette, IN 47907 USA

Abstract

A technique for reconstruction of liquid-gas interfaces based on high-speed stereo-imaging is applied to the liquid-vapor interfaces formed above a heated surface during pool boiling. Template matching is used for determining the correspondence of local features of the liquid-vapor interfaces between the two camera views. A sampling grid is overlaid on the reference image, and windows centered at each sampled pixel are compared with windows centered along the epipolar line in the target image to obtain a correlation signal. The three-dimensional coordinates of each matched pixel are determined via triangulation, which yields the physical world representation of the liquid-vapor interface.

Liquid-vapor interface reconstruction is demonstrated during pool boiling for a range of heat fluxes. Textured mushroom-like vapor bubbles that are fed by multiple nucleation sites are formed close to the heated surface. Analysis of the temporal attributes of the interface distinguishes the transition with increasing heat flux from a mode in which vapor is released from the surface as a continuous plume to one dominated by the occurrence of intermittent vapor bursts. A characteristic morphology of the vapor mushroom formed during vapor burst events is identified.

This liquid-vapor interface reconstruction technique is a time-resolved, flexible and non-invasive alternative to existing methods for phase-distribution mapping, and can be combined with other optical-based diagnostic tools, such as tomographic particle image velocimetry. Vapor flow morphology characterization during pool boiling at high heat fluxes can be used to inform vapor removal strategies that delay the occurrence of critical heat flux during pool boiling.

Nomenclature

$corr$ correlation

f focal length, mm

I image intensity, -

k_1 first radial distortion coefficient, mm^{-2}

q'' heat flux, W/cm^2

s_x pixel skew factor, -

t time, ms

T_s surface temperature, K

T_{sat} saturation temperature, K

u, v pixel coordinates, -

u_0, v_0 image principal point, -

W correlation window, -

x, y, z world coordinates, mm

x_0, y_0, z_0 camera center of projection, mm

Greek symbols

α rotation angle of camera coordinate system

about world coordinate axis, deg

θ contact angle of liquid-vapor interface, deg

Subscript

l left camera or image

r right camera or image

x x-coordinate axis

y y-coordinate axis

z z-coordinate axis

1. Introduction

Understanding two-phase flow phenomena can offer prediction capabilities relevant to a wide variety of industrial applications, such as chemical processing in bubble column reactors [1,2], phase-change-based heat exchangers [3,4], molten metal processing in gas stirred vessels [5], and aeration in waste water treatment [6] among many others [7]. Research has been devoted for decades to unveiling the complexities of these two-phase flows. Recent contributions have been related to the development of experimental techniques and computational models aimed at resolving the phase distribution and velocity fields in each phase.

Characteristics of the phase distribution in two-phase flows, including the void fraction and interfacial area concentration, are central to modeling approaches. In the seminal two-fluid model [7,8], local void fraction was used to formulate separate conservation equations for each phase via averaging in a representative volume. Mass, momentum, and energy transport between the phases are proportional to the product of the local interfacial area concentration and a driving potential. A special emphasis has been placed on the development of mechanistic models for the interfacial area concentration [7]. Other high-fidelity numerical modeling approaches have explicit representations of the interface between phases [9,10]. Detailed information regarding phase distribution obtained from experiments is required to inform and validate these modeling approaches.

An ideal measurement system to map the gaseous phase distribution and track the interface in a two-phase flow should be accurate, non-invasive, applicable to different flow configurations, easy to implement, and have high spatial and temporal resolution [11]. Multiple techniques have been developed with inherent tradeoffs among these traits, typically with an emphasis on characterizing dispersed bubbly flows. Invasive probe-based techniques take advantage of the contrast in different physical properties, such as electrical impedance [12,13], refractive index [14] or thermal transport properties [15], to instantaneously detect the phase present at a single point in the flow. Temporally-averaged phase distributions in steady-state flows can be estimated by translating the probe across the domain. As an extension of local probes, wire-mesh sensors use an electrode grid to determine the void fraction distribution over the mesh cross-section at a high temporal resolution [16,17]. Flow disruption is the main concern in the application of probes, wire-mesh sensors, or any other invasive technique.

Non-invasive tomographic approaches provide multi-dimensional information of the phase distribution but their implementation can be non-trivial and require numerical reconstruction techniques based on inverse methods, which induce uncertainty [18]. Photon-attenuation-based tomography, X-ray or gamma-ray, can estimate phase (density) distribution in complex two-phase flows, with multiple interfaces along a line of sight, due to the weak interaction for scattering between high energy photons and common fluids [19]. To lessen noise effects, most X-ray tomographic configurations use a small

focused beam that is raster-scanned through the domain, limiting the temporal resolution [16,19]. Electrical-impedance-based tomographic systems having electrodes at the wall of the tank, pipe or channel are attractive because they are easy to implement [20]. However, reconstruction is more challenging because of the complex dependence between the phase distribution and impedance. Ultrasonic-based tomography can be used in dispersed bubbly flows; however, its application is limited to low void fractions because a strong signal attenuation is induced by wave reflections at interfaces [18].

With the recent developments in high-speed and high-resolution digital imaging, direct imaging techniques can yield high-fidelity measurements for transparent fluids when visual access is available, without disrupting the flow [19,21]. Direct imaging has been primarily applied to dispersed bubbly flows, where image processing algorithms are used to identify individual bubbles [21–23]. The main challenge is accurate segmentation of individual bubbles when they appear overlapped in the captured images, which limits the application of direct imaging to flows with void fractions lower than ~10 % [21]. Direct imaging can be combined with other optical-based techniques, such as particle image velocimetry (PIV), to obtain a complete description of the flow field. Particle seeding allows the determination of velocities for the liquid phase, and, in dispersed bubbly flows, the velocity and distribution of the gaseous phase is determined via identification and tracking of single bubbles. In planar PIV, dispersed bubbles can be isolated from seeding particles using a size-based filter [24,25], or a separate imaging system operating at a different wavelength can be used to capture shadow images of the bubbles [26,27]. Also, three-dimensional liquid velocities measurement along with ellipsoidal bubble reconstruction has been achieved with a stereoscopic PIV set up to study single bubble dynamics [28].

The current investigation aims to extend the capabilities of direct imaging for gaseous phase distribution mapping beyond dispersed bubbly flows, to dynamically track complex liquid-vapor interfaces with a high-speed, flexible and non-invasive technique. The proposed technique uses template matching between stereoscopic views to reconstruct the three-dimensional interface shape; it is applicable to two-phase flow structures having rippled or otherwise textured interfaces and has the potential to be combined with other optical-based diagnostic tools, such as tomographic PIV.

The technique is applied to a particular case of pool boiling from a finite heat source, where highly textured bubbles are found near the heated surface. During pool boiling, quantitative characterization of vapor flow dynamics has been limited to discrete bubble departure at low heat fluxes [30]. At high heat fluxes, optical visualization has been generally limited to qualitative observations [31,32], except for approximation of the departure diameter of large vapor structures [33]. Conductivity probes have been used to determine the departure frequency of large vapor structures [34] and the time-averaged void fraction distribution [35]. The current work yields a unique characterization of the liquid-

vapor interface morphology near the heated surface during pool boiling at high heat fluxes, which offers insight into the vapor release mechanisms that may lead to critical heat flux.

2. Experimental methods

2.1. Experimental setup

The liquid-vapor interface reconstruction approach is applied to pool boiling from a heated surface occurring inside a sealed test section. Figure 1a is a schematic illustration of the test section for the pool boiling experiment. The walls of the test section are made of 19 mm-thick polyether ether ketone (PEEK) slabs to provide insulation. The front and rear walls have glass viewing windows of 76 mm height and 50 mm width. The 27.2 mm × 27.2 mm square heated surface is located at the bottom center of the test section and has an arithmetic average roughness of 0.63 μm. This heated surface forms the top of a copper block which consists of a top neck of small square cross-section that widens at the bottom to form a base with larger square cross-section. Twelve 150 W cartridge heaters are inserted into the base of the copper block. Rakes of T-type thermocouples (± 0.35 K) are positioned along the top neck of the copper block to determine the heat flux at the surface and extrapolate the surface temperature, assuming one-dimensional conduction.

The test section is filled with deionized water to a level of ~90 mm above the heater. The vapor generated from the boiling process is condensed on the surface of a copper coil located at the top of the test section, through which cold water flows. Two 170 W auxiliary immersion heaters are used to maintain saturated conditions inside the pool and for degassing. A pressure transducer (Omegadyne PX409) is installed to measure the pressure (and hence saturation temperature) inside the test section. The uncertainty in the saturation temperature (±0.12°C) is evaluated based on the manufacturer-quoted uncertainty for the pressure transducer. Additional details about the test section can be found in Ref. [36].

Figure 1b presents the optical setup to acquire stereoscopic images of the liquid-vapor interface during pool boiling. Images are acquired with a single high-speed camera (Phantom Veo 710L) at 2000 fps using a stereo adapter. The stereo adapter (Loreo 3D Macro LA9006) allows simultaneous capture of two different views with a single sensor, obtaining images such as those presented in Figure 1c. Front illumination is achieved with two arc lamps symmetrically positioned with respect to the front viewing window. Backlighting through the rear viewing window is achieved with an array of light emitting diodes (LEDs). The intensity of the light sources is adjusted to obtain good contrast of the texture on the front liquid-vapor interface while preserving a sharp vapor silhouette.

The stereo adapter has an approximate stereo base line of 20 mm and an adjustable focusing range of 230 to 850 mm. The closest focusing range is used and the aperture is set such that objects located 30 mm behind or in front of the center of the heated surface are in focus. The short stereo base

line, obtained by using the stereo adapter instead of a two-camera system, reduces the relative distortion between the left and right views, favoring the correlation-based stereo correspondence search (described later in Section 3.4), and decreases the incidence of occlusion [37]. However, sensitivity to changes in depth is reduced, requiring a sub-pixel resolution approach to be used during the correspondence search.

2.2. Pool boiling experimental procedure

Before running the pool boiling experiments, the test section is degassed by vigorously boiling the water in the pool using the auxiliary immersion heaters. The vapor generated is condensed in a Graham reflux condenser that is installed at the top of the facility, while non-condensable gases vent out. After degassing for ~1 hr, flow of cold water through the condenser coil is initiated and controlled to maintain a constant pressure of 1 atm inside the chamber. The valve of the Graham reflux condenser is quickly closed. The power input to the immersion heaters is reduced and kept constant during the pool boiling experiment to maintain uniform, saturated conditions in the chamber.

During the saturated pool boiling experiment, power input to the heater block is incremented in steps from 148 W to 742 W, which correspond to measured heat fluxes at the surface of 17 to 92 W/cm^2. The power input is kept constant at each heat flux setting, and the system is allowed to reach steady state. At steady state, images are acquired for a total of 4 s; temperature and pressure data are acquired for ~75 s and averaged over this steady period.

3. Liquid-vapor interface reconstruction

The liquid-vapor interface reconstruction process infers the three-dimensional interface position from the obtained stereo image pairs obtained. For this purpose, it is necessary to identify pixels in the left and right views that correspond to the same point on the interface in the physical world, which is known as the correspondence problem [11]. Once the correspondences are determined, the geometric information about the camera system, which is known from the calibration process, is used to determine the three-dimensional coordinates of the matched points among the views. The specific steps in the liquid-interface reconstruction process are described in detail in the subsections that follow.

3.1. Camera calibration procedure

In order to obtain the mapping functions for the camera system, a calibration procedure is conducted prior to the experiment with a glass dot-matrix flat target having 0.5 mm-diameter dots spaced 1.0 mm apart (Edmund Optics 59-217). For the calibration, the test section is filled with water at ambient temperature. The calibration target is placed parallel to the back wall of the test section, with the bottom line of calibration dots positioned ~5 mm above the heated surface, and translated through the depth of the volume of interest. Calibration images are taken at 2 mm increments for a total of 15 calibration planes. The calibration volume is 60 mm high, 40 mm wide, and 26 mm deep. The origin for the world

coordinate system is located at the center of the heated surface, with the axes defined as shown in Figure 1.

Correspondences between physical world coordinates and pixel coordinates in each view are fitted independently to find pinhole-camera model parameters for the resulting left and right pseudo cameras. The camera parameters consist of the position and orientation of each pseudo camera, as well as focal length, optical center, pixel size, and distortion parameters. A first estimate of the pseudo-camera parameters is obtained following the procedure outlined by Tsai [38], in which distortion effects are neglected and the pixel size and pixel coordinates for the image center are assumed to be known. The estimate is further refined using the Levenberg-Marquardt optimization algorithm [39,40]. A standard pinhole-camera model for a single optical medium is fitted; parameters of the pinhole-camera model provide enough flexibility to account for the distortion effects due to the presence of the air-glass and glass-water optical interfaces [41]. The calibration image processing and estimation of pinhole camera parameters are performed with an in-house code using MATLAB [42]. The resulting pseudo-camera parameters after the calibration procedure are summarized in Table 1 (rotations of the pseudo-camera coordinate system about world coordinate axes are assumed to be applied in the order of x, y, and then z).

3.2. Image rectification

The images captured with the high-speed camera using the stereo adapter are split vertically in stereo image pairs (left and right images) of equal width. To facilitate the correspondence search, the stereo image pairs are rectified. Image rectification allows the search of corresponding points between the images along horizontal scanlines, *i.e.*, a point in the right image that corresponds to a point in the left image will appear at the same vertical position but will have a horizontal shift. The horizontal shift in pixels in between corresponding points is known as disparity.

Image rectification is achieved through a geometric transformation of the coordinate systems of the left and right cameras. The transformation consists of a rotation that makes the optical axes of both cameras parallel to each other and perpendicular to the line connecting the centers of projection (origin of the camera coordinate system) of both cameras [43,44].

3.3. Vapor masking and feature extraction

The correspondence search is performed on feature-filtered images instead of raw grayscale images. Performing the search on feature-filtered images helps to minimize the effects of unbalanced lighting in between the left and right views that occur in grayscale images. The brightness of corresponding regions in the left and right view may differ due to uncontrollable reflections and bubble lensing effects; also, the system of mirrors in the stereo adapter induces a shadowed region near the center of the camera sensor close to the merging line for both views, as can be seen in Figure 1c.

In order to extract the features in the liquid-vapor interface, a difference-of-Gaussian filter is applied to the grayscale images. The difference-of-Gaussian filter provides a close approximation to the scale-normalized Laplacian of Gaussian [45]. For the current data, a standard deviation of 1 pixel and a non-dimensional difference of 0.1 between scales are used. The field obtained after applying the difference of Gaussian is normalized by the standard deviation in intensity of the field inside the region of interest. Then, values greater than 1.0 are saturated and set to 1, values lower than 0.1 are set to 0. Figure 2a shows a sample grayscale left image and Figure 2b presents the feature-filtered version of this image. Most features are recovered with high contrast and the observable non-uniform illumination effects are clearly attenuated. In regions with poor illumination, like the bottom right corner of the sample image, the feature detection is moderately weaker.

To accelerate the correspondence search and to eliminate sources of error in the interface reconstruction, the search is restricted to the regions covered by vapor in each frame, which are dynamically masked. In the dynamic masking algorithm, visible elements from the background are eliminated by computing the difference between the grayscale images of the two-phase flow with a background image in the absence of vapor that is taken after the boiling test with the cartridge heaters turned off. Features are extracted from the image difference following the procedure described for grayscale images. Then, a Gaussian filter with a standard deviation of 2 pixels is applied to smooth noise resulting from the feature extraction procedure, and the image is binarized to obtain the boundaries of the vapor regions. A morphological closing operation is applied with a 3 pixels × 3 pixels circular structuring element to fill small gaps in the boundaries of the vapor regions. Finally, holes inside the boundaries of the vapor regions are selectively filled. Large holes with high intensity in the grayscale images are excluded because they are likely to be either a portion of the background surrounded by vapor bubbles, or smooth regions of large bubbles without the required feature information for the correspondence search. Figure 2c presents the resulting mask for the sample image in Figure 2a. The masking process is satisfactory but has a tendency to overestimate the vapor regions. The regions falsely detected as vapor are easily filtered during the generation of a surface representation for the liquid-vapor interface (Section 3.5).

3.4. Correspondence search

Many algorithms have been proposed to estimate similarity between features on the images, establish the position of corresponding pixels, and impose smoothness assumptions [46]. In the present study, template matching based on correlation windows is used to estimate similarity between features, while a maximum correlation value criterion is used to establish the position of corresponding pixels. More complex approaches are available, such as comparison of feature descriptors that are less sensitive to distortion between views[47,48], or optimization techniques that explicitly handle surface smoothness

[49]. However, template matching has a straightforward implementation and is widely used as the baseline to evaluate proposed algorithmic improvements.

The search algorithm compares a reference window in the left feature-filtered image with windows of the same size along the respective horizontal scan line in the right feature-filtered image. Correlation of the intensity values in the feature-filtered images is used to assess the similarity between two windows. The correlation is normalized by the mean and second moment of the intensity values in each window. The correlation is computed as:

$$corr = \frac{\sum_{W}\left(I_l - \bar{I}_l\right)\left(I_r - \bar{I}_r\right)}{\sqrt{\left[\sum_{W}\left(I_l - \bar{I}_l\right)^2\right]\left[\sum_{W}\left(I_r - \bar{I}_r\right)^2\right]}} \tag{1}$$

The correspondence search on the right image is limited to the range of expected disparities assuming the liquid-vapor interfaces are in the vicinity of the heater, -150 pixels $\leq d \leq 115$ pixels. For each reference pixel centered at a window in the left image, a correlation signal is computed with windows across the horizontal scan line on the right image within the disparity limits. For the results presented, windows of 30 pixels $\times$ 30 pixels are used, and pixels in the left (reference) image are sampled with a window overlap of 90%.

The matching or corresponding pixel should be located where the correlation signal reaches a maximum peak value. However, due to the presence of noise in the feature images, several peaks of comparable value can be detected in the correlation signal, which generates ambiguity in the correspondence search. To overcome this ambiguity, an ensemble correlation signal is computed by averaging the correlation signals at each pixel from the previous three frames, the current frame, and the following three frames. The false peaks should attenuate with the averaging process, while the peak coincident with the actual matching pixel should remain.

The ensemble correlation approach is widely used in PIV to find mean displacement fields when dealing with image sequences having low particle seeding [50,51]. This approach is beneficial for the liquid-vapor interface reconstruction problem because the texture on the interface evolves at a smaller time scale than the overall shape of the interface. Hence, the information used to estimate the correlation signal is different between frames, allowing improved inference of the three-dimensional interface position that is consistent between frames.

Once the ensemble correlation is computed, the pixel coordinate in the right image corresponding to the reference pixel is determined at the maximum peak value. To achieve subpixel accuracy in the correspondence estimate, the location of the correlation peak is estimated using a quadratic fit between the peak value and the two neighboring values.

Figure 3a presents the resulting disparity field when a single-frame correlation is used on the sample frame, while Figure 3b presents the results obtained with the seven-frame ensemble correlation. In the single-frame correlation, several patches of incorrect disparity values can be identified. The seven-frame ensemble correlation corrects these patches (see lower right region of the frame at the center of the bubble at the front of the heater). Figure 3c and Figure 3d present the relative magnitude of the first peak to the second peak in the correlation signal (peak-to-peak ratio) for the single-frame correlation and seven-frame ensemble correlation, respectively. The ambiguity in peak detection is reduced with the implementation of the ensemble approach in some regions, such as the center of the bubble at the front of the heater. Remaining regions with high peak-to-peak ratio are boundary lines in between bubbles located at different depths, or regions where the ambiguity in the correspondence estimate is persistent. The most probable causes for persistent ambiguity are poor feature detection in regions with low contrast and contamination of the recovered features by ripples in an interface behind the front interface that can be seen due to transparency. This is a consequence of the transparency and specular reflectivity of vapor structures, which challenge the assumptions of opacity and diffuse reflectivity in stereo surface reconstruction.

3.5. Surface representation of the liquid-vapor interface

From each pair of corresponding pixels, the three-dimensional position of a point is computed using the geometric information of the camera system to obtain a cloud of points on the interface in space. To reconstruct the surface which corresponds to the liquid-vapor interface, a triangular mesh is chosen as a robust and simple surface representation.

The connectivity for the triangular mesh representation is established in the two-dimensional pixel domain for the set of pixels on the left image for which the disparity is estimated. Each isolated vapor region detected during the masking process is triangulated separately. Before computing the triangulation, each region is trimmed to eliminate small protruding features. If necessary, regions connected by a single pixel are split and triangulated separately.

The raw three-dimensional reconstruction of the liquid-vapor interface, represented as a triangular mesh, is shown in Figure 4a for the sample frame. Additional filtering is required to eliminate errors induced by incorrect correspondence estimates and to eliminate elements connecting bubbles that overlap in the images but are located at different depths. First, elements with high skewness and those for which the front face is not simultaneously visible in both views are eliminated. Small surface patches are then removed because they are likely to correspond to erroneous matches, tiny vapor bubbles, or noise induced in previous processing steps. Figure 4b presents the final liquid-vapor interface reconstruction for the sample frame. The reconstruction region extends vertically from the heat source up to 50 mm ($0 \text{ mm} \leq y \leq 50 \text{ mm}$), has a width of 40 mm centered around the heat source ($-20 \text{ mm} \leq x \leq 20 \text{ mm}$), and

a depth of 40 mm also centered around the heater (- 20 mm $\leq z \leq$ 20 mm). Reconstruction of interfaces beyond the calibration volume is justified by the robustness of the pinhole camera model. The liquid-interface reconstruction is validated by imaging spherical representative samples, as described in the Appendix.

4. Results and discussion

4.1. Three-dimensional reconstruction of liquid-vapor interfaces

Figure 5 shows three-dimensional reconstruction results for a sequence of frames in which a large vapor structure grows and detaches from the heat source, while small and tiny vapor bubbles rise The sample frame used to describe the reconstruction process (Section 3) is taken as the initial frame, $t = 0$ ms. At this initial time, it can be seen in the grayscale images that the vapor structure attached to the surface, labeled as A, extends across the heat source width and has an irregular shape with a medium-sized bump on the right and two small bumps on the left. The three-dimensional reconstruction (Figure 5b and Figure 5c) for the large vapor structure adequately captures the irregular shape of the interface, exhibiting three bumps, and the necking of the interface towards the contact line with the heat source edge. Good three-dimensional reconstruction results are obtained from regions where the interface is textured, and the texture is captured with adequate contrast in the grayscale images. For example, the connecting meniscus is composed of many tiny vapor structures that originate on the heated surface and feed the large vapor structure. The tiny vapor structures provide a texture pattern that enables matching in the correspondence search. On the top part of the vapor structure, ripples on the liquid-vapor interface resulting from flow interactions are the features matched in the correspondence search. Poor feature detection occurs on the right edge of the left view and on the left edge of the right view because the optics in the stereo adapter cast a shadow near the line that divides both views on the camera sensor (see in Figure 1c); this introduces some minor artifacts in the reconstruction at the right bottom of the medium size bump and at the left-most small bump (Figure 5b and Figure 5c). Near the center of the medium-sized bump at the right of the frame, a patch is missing in the interface reconstruction. In this region, a bright spot with poor feature contrast is captured, caused by backlighting and bubble lensing effects; moreover, ambiguity is induced in the correspondence search because features from the rear interface are captured along with features from the front interface.

Also at the initial frame, $t = 0$ ms, a small bubble labeled as B is growing and departing from the heater as an elongated vapor slug behind the large vapor structure (bubble A) on the left. Above and behind the vapor structure (bubble A) on the right of the frame, two small bubbles are rising and are labeled as C and D, one behind the other. The small bubbles B, C and D are rather smooth with little texture on the interface to match. The correspondence is mainly established between the silhouettes on

11

both views and grayscale intensity gradients caused by the illumination and bubble lensing effects. Hence, these small bubbles are reconstructed as jagged surface patches confined to a narrow depth interval that can be used for estimation of the bubbles location in space. The tiny bubbles in the upper part of the grayscale image are absent in the three-dimensional reconstruction because they are filtered along with small noisy interface patches during the generation of a surface representation of the interface, as described in Section 3.5.

As time progresses, the vapor structure (bubble A) grows ($t = 15$ ms), and its shape becomes similar to a mushroom cap as the meniscus connecting to the heated surface starts to detach ($t = 30$ ms). As the vapor structure starts to detach form the surface ($t = 30$ ms), the interface becomes smooth enough that grayscale intensity gradients due to illumination dominate in the correspondence search and the vapor structure interface is reconstructed as a set of jagged patches. In the region close to the surface, the meniscus attached to the heat source edge is adequately reconstructed. The interface geometry and dynamics are best captured near the heat source, where the boiling behavior generates distinctive features that can be appropriately matched between left and right views.

4.2. *Behavior of liquid-vapor interface near the heated surface during pool boiling*

Table 2 lists the heat fluxes for the pool boiling cases considered, along with the corresponding surface superheat (difference between the heated surface temperature and the saturation temperature). The observed heat transfer behavior is consistent with the well-known behavior for nucleate pool boiling. Most of the pool boiling cases considered lie in a regime with growing vapor mushroom structures. In this regime, vapor structures are formed near the heated surface by the coalescence of vapor bubbles from neighboring nucleation sites. The 'vapor mushroom' term is used to describe such vapor structures when they are attached to the heated surface and fed by several columnar stems of vapor [32]. After a vapor mushroom leaves the surface, vapor again accumulates on the surface and new vapor mushrooms grow and coalesce.

At the lowest heat flux for which the liquid-vapor interface is reconstructed, 36 W/cm^2, vapor mushrooms typically leave the surface as medium-sized bubbles, with widths comparable to half of the heat source side dimension, as can be seen in the sequence of grayscale images in Figure 6a. These bubbles form and rise frequently in groups, forming a plume strongly dominated by upward buoyancy forces. As the heat flux increases, vapor mushrooms become larger before departing from the surface and fan out beyond the heat source footprint. When large vapor structures depart, a strong trailing wake entrains vapor from the heated surface, forming a trailing slug which efficiently strips most vapor from the heater before new vapor mushroom structures again grow. At the highest heat fluxes such as 82 W/cm^2, the formation and departure of large vapor mushrooms dominates, with bursts of vapor periodically leaving the surface (see sequence of grayscale images in Figure 7a, supplementary videos

with grayscale images and interface reconstructions for heat fluxes of 36 and 82 W/cm^2 are available online).

Figure 6b and Figure 7b present a sequence of liquid-vapor interface reconstruction results for heat fluxes of 36 and 82 W/cm^2, respectively. The reconstruction adequately captures the general dynamics of the liquid-vapor interface near the heated surface. The front interface of the newly formed mushroom bubbles is consistently well reconstructed, as are lower portions of the larger mushroom bubbles where the meniscus connects to the heater surface. As the bubbles grow and depart from the surface, the liquid-vapor interface reconstruction further away from the heater is prone to the artifacts described in Section 4.1. Liquid-interface reconstruction fails for the lowest experimental heat flux, 17 W/cm^2, for which bubbles above the heater are small and without sufficient texture for their front interface to be reconstructed as a curved surface.

The median contact angle of the interface attached to the front edge of the heated surface is computed from reconstruction results in a region that extends 0.5 mm above the surface. The contact angle is defined as the angle between the interface and the heated surface measured across the liquid phase. When the vapor is removed from the heated surface and the interface recedes inwards toward the heat source, the contact angle tends to 180° (cos θ = -1). Conversely, when the vapor structures grow and extend beyond the heated footprint, the contact angle tends to 0° (cos θ = 1). The cosine of the contact angle is determined based on the dot product of the reconstructed interface normal and the heated surface normal. However, when the vapor structures extend beyond the heated surface footprint and the contact angle is very low, the portion of the interface that attaches to the heated surface is not reconstructed due to visibility constraints. When this occurs, an approximation of this portion of the interface is found by connecting the reconstruction results to the heater edge. Hence, the contact angle is estimated from triangular elements 0.5 mm or less above the heated surface as the angle formed by the shortest ray connecting the centroid of the element and the heater front edge with the heated surface plane.

Figure 6c and Figure 7c present the temporal behavior of the cosine of the median contact angle of the liquid vapor interface attached to the front edge of the heater, shown for heat fluxes of 36 W/cm^2 and 82 W/cm^2, respectively. For the heat flux of 36 W/cm^2, the cosine of the contact angle signal has random fluctuations that are confined to a narrow range of mostly negative values, which is consistent with the observations from the grayscale images and the reconstructions of the vapor flowing in a plume dominated by buoyancy forces. For the heat flux of 82 W/cm^2, several events having similar characteristics are observed in the signal; the cosine of the contact angle rises quickly to a value close to unity, remains constant for some time, and then falls. These events correspond to the release of vapor bursts, for which large vapor mushrooms quickly form and hover over the surface before departing. The different behavior for the two cases is highlighted in their probability density functions for the cosine of

the contact angle, presented in Figure 6d and Figure 7d. As the heat flux increases, the probability density function changes from a narrow and symmetric unimodal distribution to a wider distribution with a dominant peak near unity. The dominant peak close to unity for high heat fluxes is associated with the more frequent vapor burst events.

4.3. Liquid-vapor interface morphology during vapor burst

During vapor burst events, large vapor mushrooms hover over the heated surface, preventing the liquid from rewetting the surface. Hydrodynamic theories [52,53] predict that critical heat flux will occur when the liquid macrolayer underneath the vapor mushroom depletes during the hovering time, which causes blanketing of the heated surface with vapor. Hence, characterization of the vapor burst release mechanism can provide insight into the critical heat flux phenomenon. At high heat fluxes, the vapor burst events have a characteristic signature in the cosine of the contact angle signals. This characteristic signature indicates that the liquid-vapor interface undergoes similar morphological changes during the evolution of the vapor burst events. The interface morphology evolution of a characteristic vapor burst event is studied by combining interface reconstruction results for a set of vapor burst events extracted from the 82 W/cm^2 and 92 W/cm^2 heat flux cases.

The interface morphology of the characteristic vapor burst event is constructed by averaging reconstruction results for 33 vapor burst events aligned in time. Figure 8 presents the alignment of the interface contact angle signatures over all events, and confirms the similarity of the vapor burst events. The resulting average signature and bounds at one standard deviation are also presented. The average time that the liquid-vapor interface is pinned to the front edge of the heater is 26.7 ms, defined as the duration of the plateau in the cosine of the contact angle signal.

Figure 9 presents the evolution of the interface morphology for the characteristic vapor burst event. The formation of the vapor mushroom starts with detachment of the previous vapor mushroom and the development of a thin layer of vapor covering the heated surface ($t = $ -15 ms). The thin layer is slightly non-uniform, with accumulation of vapor at the heat source corners because the detachment of the previous vapor mushroom progresses from the corners to the center of the heater. Hence, the new vapor layer develops first at the corners. As the vapor layer continues to grow, the accumulation of vapor at the corners accentuates, and the layer evolves into a lobed vapor structure that fans out beyond the heater footprint ($t = 0$ ms). Finally, the lobed vapor structure begins to detach, which causes the meniscus to recede ($t = 15$ ms). The interface lobed morphology is a consequence of the square shape of the heater, which favors the accumulation of vapor at the corners during the initial vapor mushroom formation. This finding warrants further investigation of the relation between the vapor mushroom morphology identified and the hovering time, as well as the effects of heater shape on the morphology and removal of vapor from the heated surface.

14

5. Conclusion

A liquid-vapor interface reconstruction technique using high-speed stereo imaging is implemented and applied to textured vapor structures formed above a finite heated surface during pool boiling. The technique extends the capabilities of using direct imaging for non-invasive three-dimensional phase-distribution mapping beyond dispersed bubbly flows, and is inherently compatible with other optical-based flow characterization techniques, such as tomographic PIV. The reconstruction procedure relies on feature extraction and matching between stereo views to establish the three-dimensional coordinates of points lying on the liquid-vapor interface, and consequently requires textured interfaces. The feature correspondence search benefits from the use of ensemble correlation, which helps to attenuate the effects of false matches due to transparency effects and poor detection of features in low-contrast regions of the images. For textured interfaces close to the heated surface, an appropriate surface representation of the liquid-vapor interfaces is obtained that is suited to studying interface dynamics. The feasibility of using stereo imaging for three-dimensional phase distribution mapping is demonstrated using a straightforward implementation of template matching. Modifications in the optical set up can also advance the capabilities of the reconstruction technique; these include expanding the spatial and angular coverage with the utilization of more high-speed camera and stereo adapter sets.

The interface reconstruction technique is applied to mushroom-like vapor structures on top of the heated surface during pool boiling for a range of heat fluxes. The reconstruction technique produces good results for liquid-vapor interfaces close to the heated surface, where the interface is highly textured. Hence, the front interface of small vapor mushrooms attached to the heated surface, and the lower part of large vapor mushrooms where the meniscus connects to the surface, are appropriately captured. As the vapor mushrooms detach from the surface, the interface becomes smooth and the reconstruction results deteriorate. A transition is observed in the nature of the vapor structures with increasing heat flux from a plume-like vapor flow to a vapor release mode dominated by vapor burst events. The transition is discernible in the temporal data for the cosine of the contact angle of the interface attached to front edge of the heat source, in which the vapor burst events have a characteristic signature. The probability density distributions for the cosine of the contact angle signals also reveal a clear distinction between the continuous vapor plume and vapor burst mode. For the continuous vapor plume release mode, the distribution is unimodal and restricted to a narrow range, while for the vapor burst mode, the distribution has a larger spread with a dominant peak near unity. A characteristic morphology evolution of the vapor structures during vapor burst events is identified. The square shape of the heater favors the accumulation of vapor at the corners at the early stages of the formation of large vapor mushrooms, which results in the development of lobed structures.

Acknowledgements

Appendix

Supplementary data associated with this article can be found in the online version.

References

[1] N. Kantarci, F. Borak, and K. O. Ulgen, "Bubble column reactors," *Process Biochem.*, vol. 40, pp. 2263–2283, 2005.

[2] A. Shaikh and M. Al-Dahhan, "Scale-up of bubble column reactors: A review of current state-of-the-art," *Ind. Eng. Chem. Res.*, vol. 52, pp. 8091–8108, 2013.

[3] S. G. Kandlikar, "A general correlation for saturated two-phase flow boiling heat transfer inside horizontal and vertical tubes," *J. Heat Transfer*, vol. 112, no. 1, pp. 219–228, 1990.

[4] X. F. Peng and B.-X. Wang, "Forced convection and flow boiling heat transfer for liquid flowing through microchannels," *Int. J. Heat Mass Transf.*, vol. 36, no. 14, pp. 3421–3427, 1993.

[5] M. P. Schwarz, "Simulation of gas injection into liquid melts," *Appl. Math. Model.*, vol. 20, no. 1, pp. 41–51, 1996.

[6] F. A. Bombardelli, G. C. Buscaglia, C. R. Rehmann, L. E. Rincón, and M. H. García, "Modeling and scaling of aeration bubble plumes: A two-phase flow analysis," *J. Hydraul. Res.*, vol. 45, no. 5, pp. 617–630, 2007.

[7] M. Ishii and T. Hibiki, *Thermo-Fluid Dynamics of Two-Phase Flow*. New York, NY: Springer New York, 2011.

[8] I. Kataoka, M. Ishii, and A. Serizawa, "Local formulation and measurements of interfacial area concentration in two-phase flow," *Int. J. Multiph. Flow*, vol. 12, no. 4, pp. 505–529, 1986.

[9] A. Prosperetti and G. Tryggvason, *Computational methods for multiphase flows*. Cambridge, New York: Cambridge University Press, 2007.

[10] G. Tryggvason, R. Scardovelli, and S. Zaleski, *Direct numerical simulations of gas-liquid multiphase flows*. Cambridge, New York: Cambridge University Press, 2011.

[11] F. Bellocchio, N. A. Borghese, S. Ferrari, V. Piuri, and S. Reconstruction, *3D Surface Reconstruction*. New York, NY: Springer New York, 2013.

[12] Y. Liu, X. Yang, Q. Zhu, P. Ju, M. Ishii, and J. R. Buchanan, "Development of the droplet-capable conductivity probe for measurement of liquid-dispersed two-phase flow," *Int. J. Multiph. Flow*, vol. 88, pp. 238–250, 2017.

[13] S. Kim, X. Y. Fu, X. Wang, and M. Ishii, "Development of the miniaturized four-sensor conductivity probe and the signal processing scheme," *Int. J. Heat Mass Transf.*, vol. 43, no. 22, pp. 4101–4118, 2000.

[14] F. Murzyn, D. Mouaze, and J. R. Chaplin, "Optical fibre probe measurements of bubbly flow in hydraulic jumps," *Int. J. Multiph. Flow*, vol. 31, no. 1, pp. 141–154, 2005.

[15] B. Farrar, A. L. Samways, J. Ali, and H. H. Bruun, "A computer-based hot-film technique for two-phase flow measurements," *Meas. Sci. Technol.*, vol. 6, pp. 1528–1537, 1995.

[16] H. M. Prasser, M. Misawa, and I. Tiseanu, "Comparison between wire-mesh sensor and ultra-fast X-ray tomograph for an air-water flow in a vertical pipe," *Flow Meas. Instrum.*, vol. 16, no. 2–3, pp. 73–83, 2005.

[17] M. J. Da Silva ., S. Thiele, L. Abdulkareem, B. J. Azzopardi, and U. Hampel, "High-resolution gas-oil two-phase flow visualization with a capacitance wire-mesh sensor," *Flow Meas. Instrum.*, vol. 21, no. 3, pp. 191–197, 2010.

[18] C. Boyer, A. M. Duquenne, and G. Wild, "Measuring techniques in gas-liquid and gas-liquid-solid reactors," *Chem. Eng. Sci.*, vol. 57, no. 16, pp. 3185–3215, 2002.

[19] A. Kastengren and C. F. Powell, "Synchrotron X-ray techniques for fluid dynamics," *Exp. Fluids*, vol. 55, no. 3, 2014.

[20] S. Paranjape, S. N. Ritchey, and S. V. Garimella, "Electrical impedance-based void fraction measurement and flow regime identification in microchannel flows under adiabatic conditions," *Int. J. Multiph. Flow*, vol. 42, pp. 175–183, 2012.

[21] Y. Fu and Y. Liu, "Experimental study of bubbly flow using image processing techniques," *Nucl. Eng. Des.*, vol. 310, pp. 570–579, 2016.

[22] M. Honkanen, P. Saarenrinne, T. Stoor, and J. Niinimäki, "Recognition of highly overlapping

ellipse-like bubble images," *Meas. Sci. Technol.*, vol. 16, no. 9, pp. 1760–1770, 2005.

[23] W. Cheng, Y. Murai, T. Sasaki, and F. Yamamoto, "Bubble velocity measurement with a recursive cross correlation PIV technique," *Flow Meas. Instrum.*, vol. 16, no. 1, pp. 35–46, 2005.

[24] M. J. Sathe, C. S. Mathpati, S. S. Deshpande, Z. Khan, K. Ekambara, and J. B. Joshi, "Investigation of flow structures and transport phenomena in bubble columns using particle image velocimetry and miniature pressure sensors," *Chem. Eng. Sci.*, vol. 66, no. 14, pp. 3087–3107, 2011.

[25] M. Sathe, J. Joshi, and G. Evans, "Characterization of turbulence in rectangular bubble column," *Chem. Eng. Sci.*, vol. 100, pp. 52–68, 2013.

[26] A. Tokuhiro, M. Maekawa, K. Iizuka, K. Hishida, and M. Maeda, "Turbulent flow past a bubble and an ellipsoid using shadow-image and PIV techniques," *Int. J. Multiph. Flow*, vol. 24, no. 8, pp. 1383–1406, 1998.

[27] M. J. Sathe, I. H. Thaker, T. E. Strand, and J. B. Joshi, "Advanced PIV/LIF and shadowgraphy system to visualize flow structure in two-phase bubbly flows," *Chem. Eng. Sci.*, vol. 65, no. 8, pp. 2431–2442, 2010.

[28] Y. a. Hassan, J. Ortiz-Villafuerte, and W. D. Schmidl, "Three-dimensional measurements of single bubble dynamics in a small diameter pipe using stereoscopic particle image velocimetry," *Int. J. Multiph. Flow*, vol. 27, pp. 817–842, 2001.

[29] R. S. Patel and S. V. Garimella, "Technique for quantitative mapping of three-dimensional liquid–gas phase boundaries in microchannel flows," *Int. J. Multiph. Flow*, vol. 62, pp. 45–51, 2014.

[30] J. P. Mchale and S. V. Garimella, "Nucleate boiling from smooth and rough surfaces – Part 2 : Analysis of surface roughness effects on nucleate boiling," *Exp. Therm. Fluid Sci.*, vol. 44, pp. 439–455, 2013.

[31] J. W. Westwater and J. G. Santangelo, "Photographic Study of Boiling," *Ind. Eng. Chem.*, vol. 47, no. 8, pp. 1605–1610, 1955.

[32] R. F. Gaertner, "Photographic Study of Nucleate Pool Boiling on a Horizontal Surface," *J. Heat Transfer*, vol. 87, p. 17, 1965.

[33] T. Kumada, H. Sakashita, and H. Yamagishi, "Pool boiling heat transfer-I. Measurement and semi-empirical relations of detachment frequencies of coalesced bubbles," *Int. J. Heat Mass Transf.*, vol. 38, no. 6, pp. 969–977, 1995.

[34] A. M. Bhat, J. S. Saini, and R. Prakash, "Role of macrolayer evaporation in pool boiling at high heat flux," *Int. J. Heat Mass Transf.*, vol. 29, no. 12, pp. 1953–1961, 1986.

[35] Y. Iida and K. Kobayasi, "Distributions of void fraction above a horizontal heating surface in pool boiling," *Bull. JSME*, vol. 12, no. 50, pp. 283–290, 1969.

[36] T. P. Allred, J. A. Weibel, and S. V. Garimella, "Enabling Highly Effective Boiling from Superhydrophobic Surfaces Taylor," *Phys. Rev. Lett.*, vol. 120, p. 174501, 2018.

[37] L. H. Quam, "Hierarchical warp stereo," *Readings in computer vision*. pp. 80–86, 1984.

[38] R. Tsai, "A versatile camera calibration technique for high accuracy 3D machine vision metrology using off-the-shelf TV cameras and lenses," *IEEE J. Robot. Autom.*, vol. 3, no. 4, p. 32344, 1987.

[39] K. Levenberg, "A method for the solution of certain non-linear problems in least squares," *Q. Appl. Math.*, vol. 2, no. 2, pp. 164–168, 1944.

[40] D. W. Marquardt, "An algorithm for least-squares estimation of nonlinear parameters," *J. Soc. Ind. Appl. Math.*, vol. 11, no. 2, pp. 431–441, 1963.

[41] B. Wieneke, "Stereo-PIV using self-calibration on particle images," *Exp. Fluids*, vol. 39, no. 2, pp. 267–280, 2005.

[42] "MATLAB." The Mathworks, Inc., Natick, Massachusetts, 2016.

[43] E. Trucco and A. Verri, *Introductory Techniques for 3-D Computer Vision*. Upper Saddle River, New Jersey: Prentice Hall, 1998.

[44] D. V. Papadimitriou and T. J. Dennis, "Epipolar line estimation and rectification for stereo image pairs," *IEEE Trans. Image Process.*, vol. 5, no. 4, pp. 672–676, 1996.

[45] D. G. Lowe, "Distinctive image features from scale-invariant keypoints," *Int. J. Comput. Vis.*, vol.

60, no. 2, pp. 91–110, 2004.

[46]   D. S. Szeliski, "A Taxonomy and Evaluation of Dense Two-Frame Stereo Correspondence Algorithms," *Int. J. Comput. Vis.*, vol. 47, no. 1–Mar, pp. 7–42, 2002.

[47]   A. Vedaldi, "An implementation of SIFT detector and descriptor," *Int. J.*, vol. 1, pp. 1–7, 2008.

[48]   E. Tola, V. Lepetit, P. Fua, and S. Member, "DAISY: An efficient dense descriptor applied to wide-baseline stereo.pdf," *IEEE Trans. Pattern Anal. Mach. Intell.*, vol. 32, no. 5, pp. 815–830, 2010.

[49]   L. Alvarez, J. Weickert, and J. Sánchez, "Reliable estimation of dense optical flow fields with large displacements," *Int. J. Comput. Vis.*, vol. 39, no. 1, pp. 41–56, 2000.

[50]   J. G. Santiago, S. T. Wereley, C. D. Meinhart, D. J. Beebe, and R. J. Adrian, "A particle image velocimetry system for microfluidics," *Exp. Fluids*, vol. 25, no. 4, pp. 316–319, 1998.

[51]   C. Willert, "Adaptive PIV processing based on ensemble correlation," in *14Th International Symposium on Applications of Laser Techniques to Fluid Mechanics*, 2008.

[52]   Y. Haramura and Y. Katto, "A new hydrodynamic model of critical heat flux, applicable widely to both pool and forced convection boiling on submerged bodies in saturated liquids," *Int. J. Heat Mass Transf.*, vol. 26, no. 3, pp. 389–399, 1983.

[53]   T. Kumada and H. Sakashita, "Pool boiling heat transfer-II. Thickness of liquid macrolayer formed beneath vapor masses," *Int. J. Heat Mass Transf.*, vol. 38, no. 6, pp. 979–987, 1995.

List of tables

List of figures

Table 1. Pinhole-camera model parameters obtained after calibration of the camera system.

Camera	Center of projection [mm]			Rotation angles [deg]			Focal length [mm]	Image center [-]		Pixel skew [-]	Radial distortion [mm^{-2}]
	x_0	y_0	z_0	α_x	α_y	α_z	f	u_0	v_0	s_x	k_1
Left	-7.3	34.7	342.1	1.1	172.1	-0.2	66.2	788.1	319.0	1.00	5.2×10^{-5}
Right	13.1	35.4	341.8	0.7	192.1	0.2	65.9	-304.2	332.7	1.00	4.5×10^{-5}

Table 2. Experimental pool boiling cases.

Heat flux q'' [W/cm^2]	Surface superheat, $T_s - T_{sat}$ [K]
17	10.6
36	12.1
54	13.3
64	13.9
73	14.4
82	15.0
92	15.4
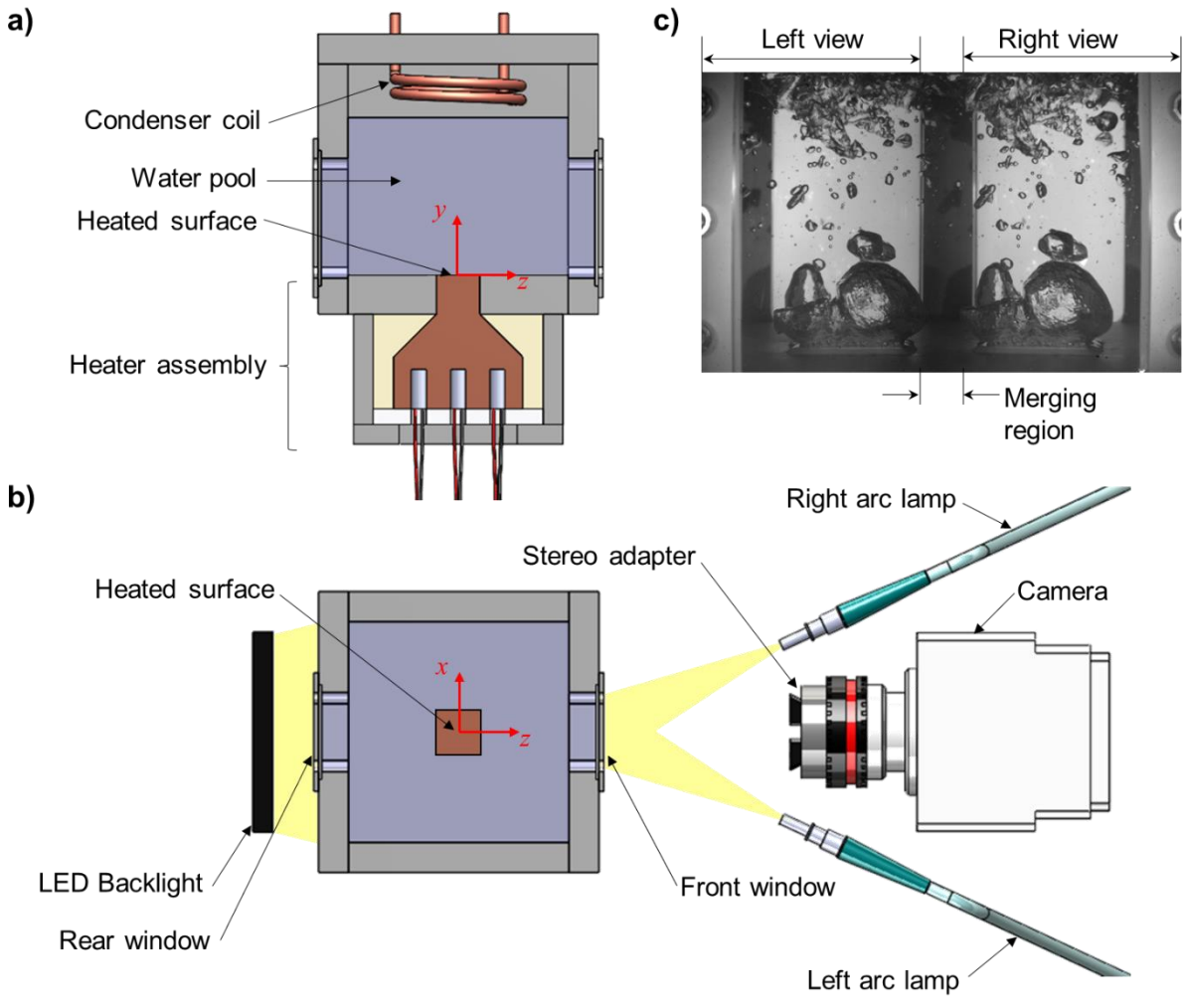
Figure 1. Schematic illustration of (a) the pool boiling experimental set up, (b) optical equipment, and (c) a sample grayscale stereoscopic image at 73 W/cm^2.
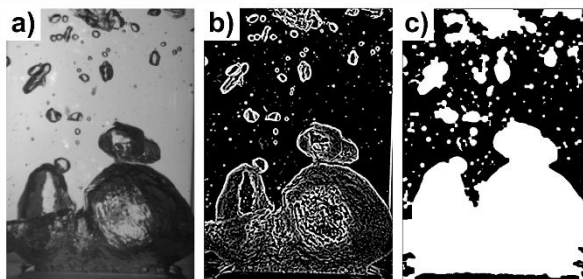
Figure 2. Sample (a) original left grayscale image, (b) featured-filtered image, and (c) vapor mask at 73 W/cm^2 (left view cropped to the region of interest).
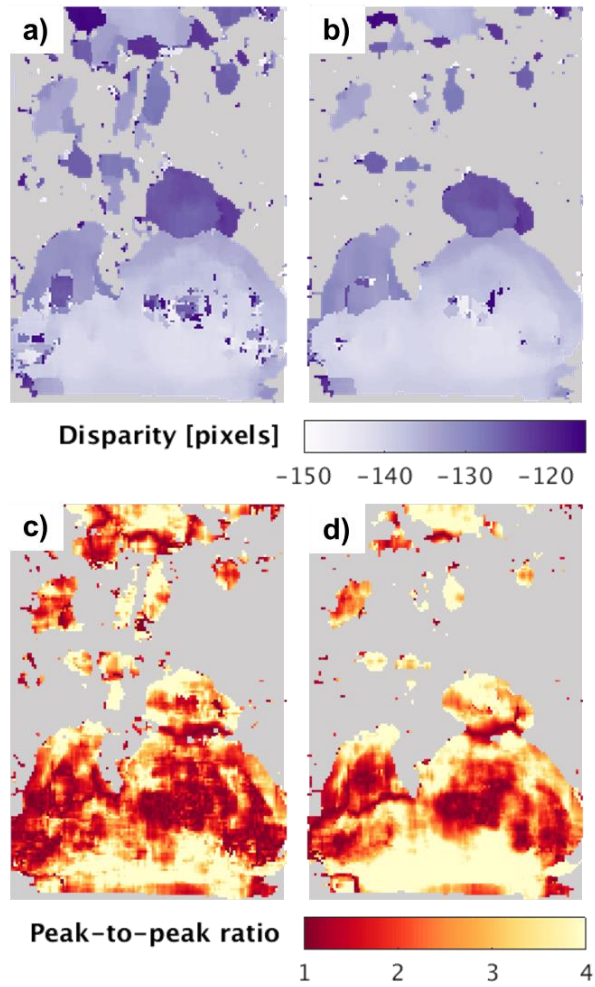
Figure 3. Disparity estimates with correlation-based template matching for (a) a single frame and (b) seven-frame ensemble correlation; ratio between first and second peak correlation values for (c) a single frame and (d) seven-frame ensemble correlation (shown for sample stereoscopic image at 73 W/cm^2).
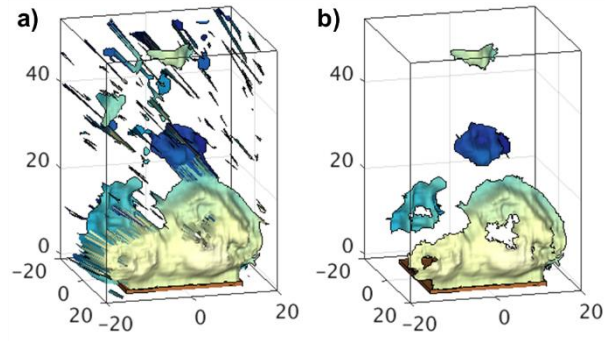
Figure 4. Three-dimensional views of reconstructed liquid-vapor interface (a) before and (b) after filtering based on the visibility constraint, element skewness, and size of surface patch (shown for sample stereoscopic image at 73 W/cm^2).
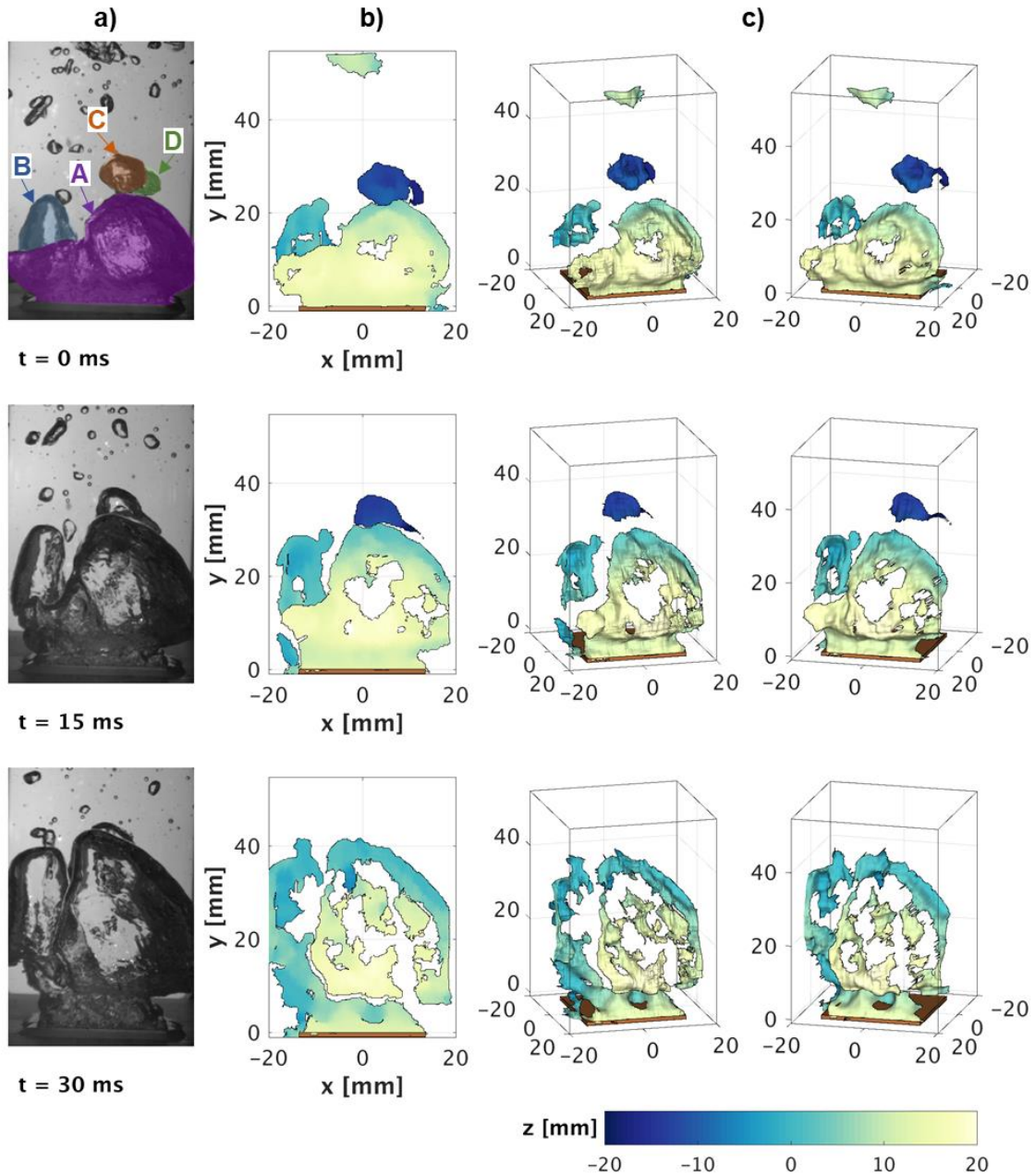
Figure 5. Sequence of (a) left grayscale images, (b) reconstructed map of the interface depth, and (c) three-dimensional views (as observed from two different angles) of the reconstructed interface for the growth of a mushroom-like bubble on top of the heated surface at 73 W/cm^2.
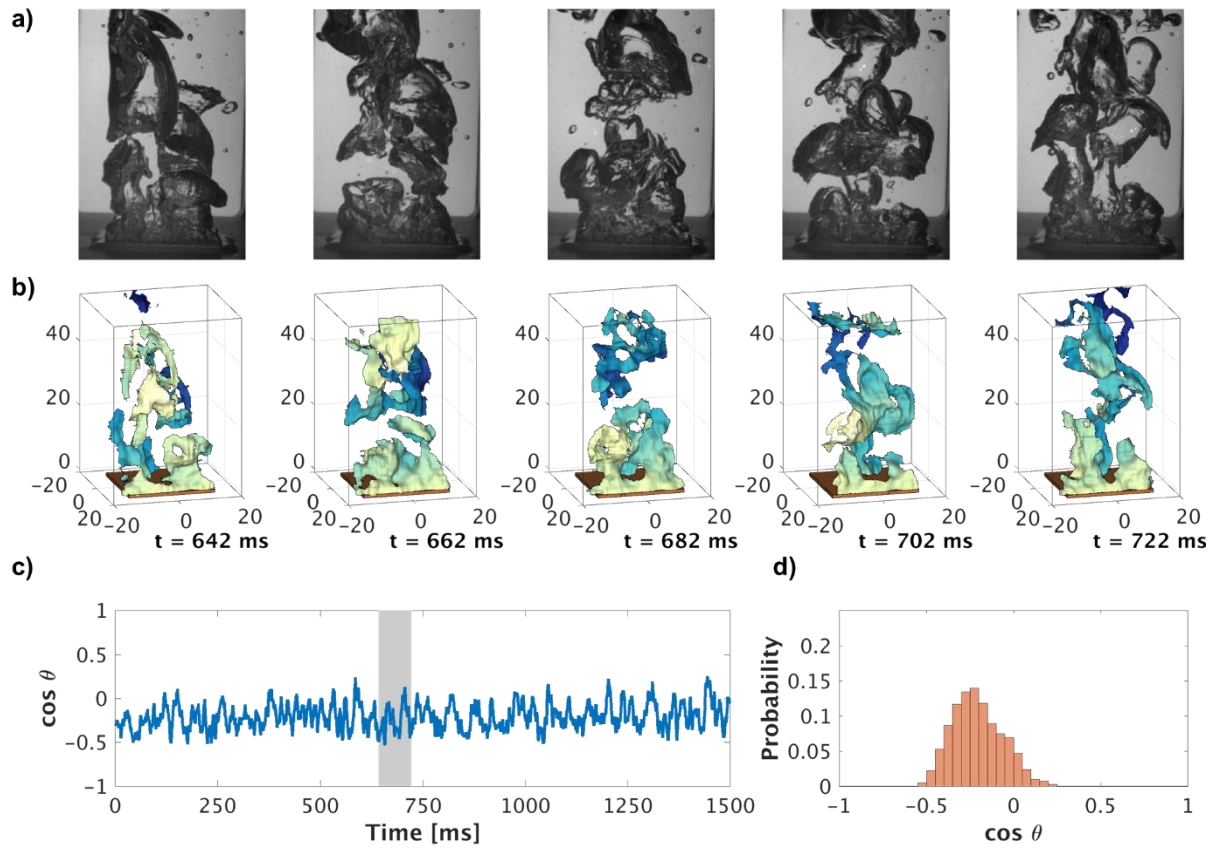
Figure 6. Sequence of (a) left grayscale images and (b) three-dimensional views of reconstructed liquid-vapor interface for a heat flux of 36 W/cm^2, as well as the (c) time signal and (d) probability density function for the cosine of the contact angle of the liquid vapor interface attached to the front edge of the heat source. Video of the grayscale images and reconstructions is available online.
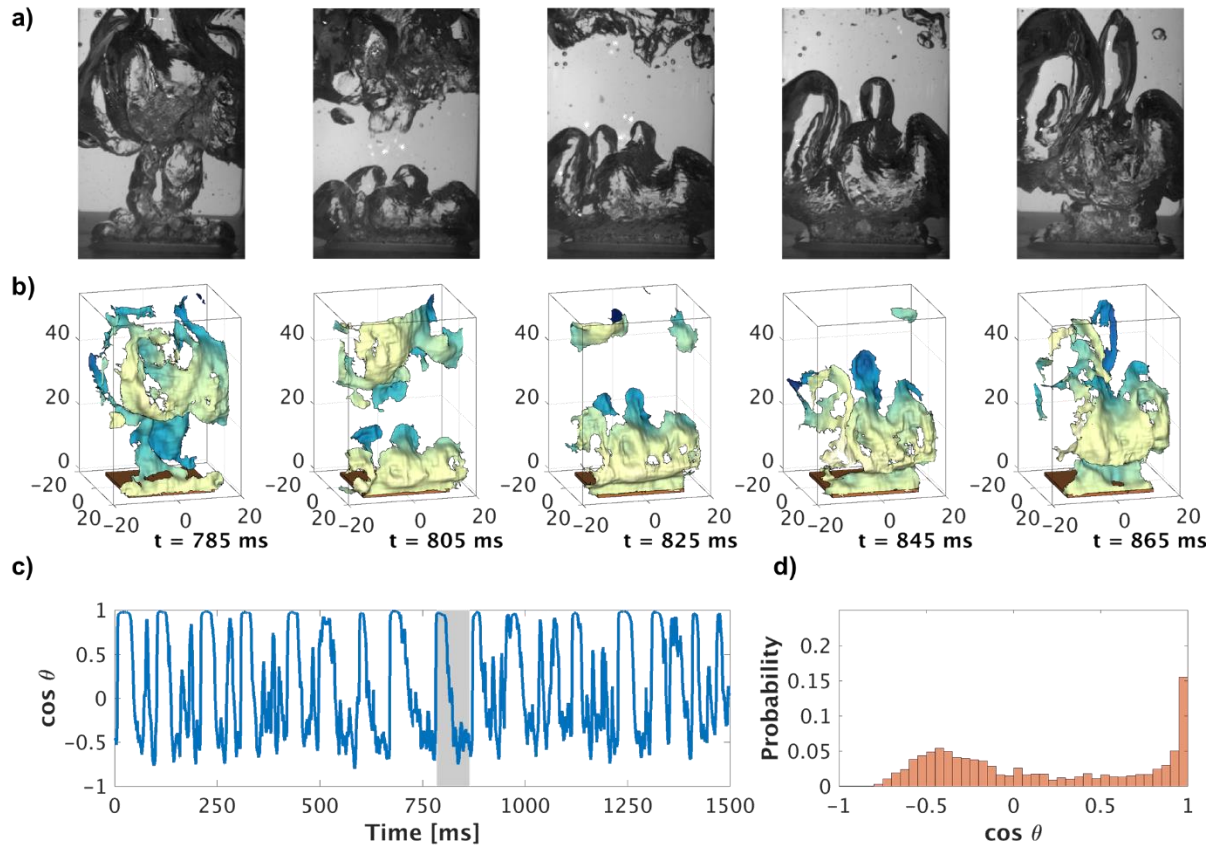
Figure 7. Sequence of (a) left grayscale images and (b) three-dimensional views of reconstructed liquid-vapor interface for a heat flux of 82 W/cm², as well as the (c) time signal and (d) probability density function for the cosine of the contact angle of the liquid vapor interface attached to the front edge of the heater. Video of the grayscale images and reconstructions is available online.
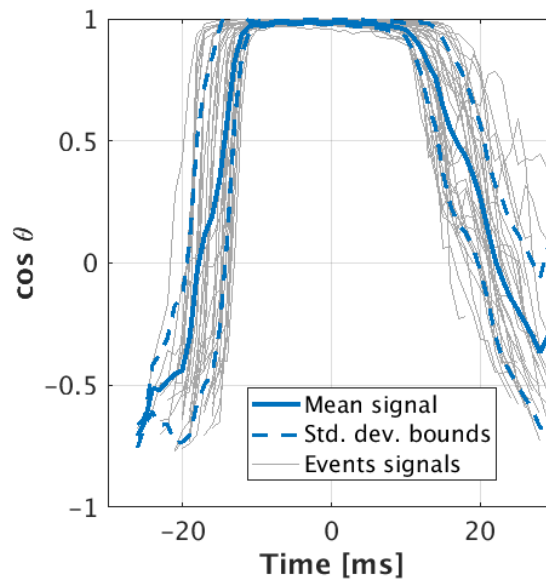
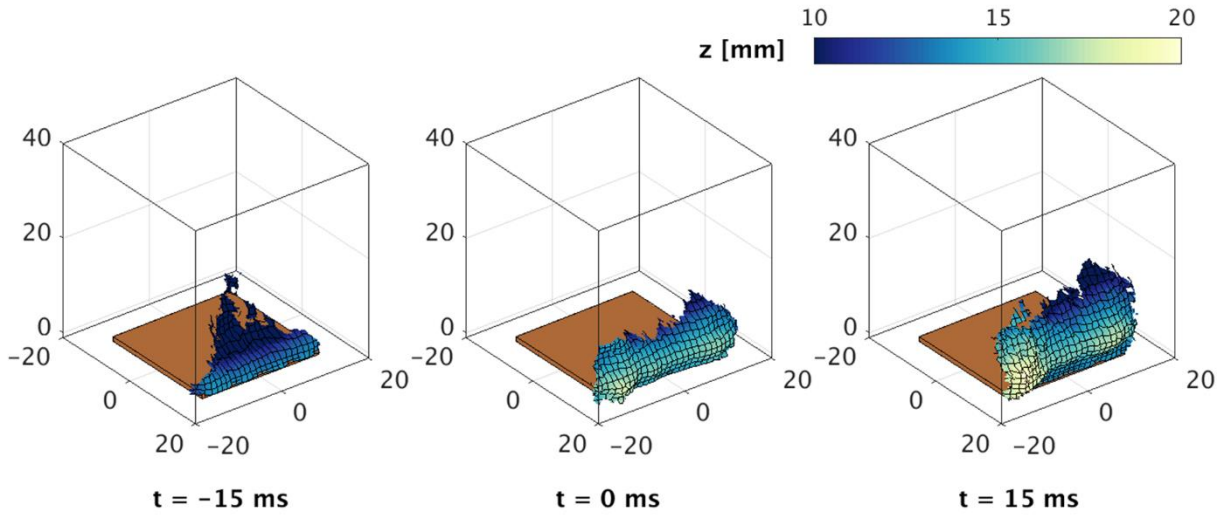Figure 8. Cosine of contact angle signals for 33 similar vapor burst events aligned in time.

Figure 9. Evolution of the interface morphology for the characteristic vapor burst event.